

## Dust Aerosol Optical Depth Retrieval over a Desert Surface Using the SEVIRI Window Channels

BART DE PAEPE AND STEVEN DEWITTE

*Vrije Universiteit Brussel, and Royal Meteorological Institute of Belgium, Brussels, Belgium*

(Manuscript received 8 January 2008, in final form 21 August 2008)

### ABSTRACT

The authors present a new algorithm to retrieve aerosol optical depth (AOD) over a desert using the window channels centered at 8.7, 10.8, and 12.0  $\mu\text{m}$  of the Spinning Enhanced Visible and Infrared Imager (SEVIRI) instrument on board the Meteosat Second Generation satellite. The presence of dust aerosols impacts the longwave outgoing radiation, allowing the aerosols over the desert surfaces to be detected in the thermal infrared (IR) wavelengths. To retrieve the aerosol properties over land, the surface contribution to the satellite radiance measured at the top of the atmosphere has to be taken into account. The surface radiation depends on the surface temperature, which is characterized by a strong diurnal variation over the desert, and the surface emissivity, which is assumed to be constant over a time span of 24 h. The surface emissivity is based on clear-sky observations that are corrected for atmospheric absorption and emission. The clear-sky image is a composite of pixels that is characterized by the highest brightness temperature (BT) of the SEVIRI channel at 10.8  $\mu\text{m}$ , and by a negative BT difference between the channels at 8.7 and 10.8  $\mu\text{m}$ . Because of the lower temperatures of clouds and aerosols compared to clear-sky conditions, the authors assume that the selected pixel values are obtained for a clear-sky day. A forward model is used to simulate the thermal IR radiation transfer in the dust layer. The apparent surface radiation for the three window channels in the presence of aerosols is calculated as a function of the surface emissivity and the surface temperature, the aerosol layer temperature, and the AOD for different aerosol loadings. From these simulations two emissivity ratios, which are stored in lookup tables (LUT), are calculated. The retrieval algorithm consists of processing the clear-sky image and computing the surface emissivity, processing the instantaneous image, and computing the apparent surface radiation for the three window channels. The two emissivity ratios are computed using the radiances at 8.7 and 10.8  $\mu\text{m}$  and at 8.7 and 12.0  $\mu\text{m}$ , respectively. The SEVIRI AOD is obtained by the inversion of these emissivity ratios using the corresponding LUT. The algorithm is applied to a minor dust event over the Sahara between 19 and 22 June 2007. For the validation the SEVIRI AOD is compared with the AOD from the Cloud Aerosol Lidar and Infrared Pathfinder Satellite Observations (CALIPSO) along the satellite track.

### 1. Introduction

The desert is the source region of dust aerosols. Throughout the year background dust aerosols are present in only small concentrations over the desert regions. Furthermore, the desert is characterized by periodical outbreaks of dust storms that transport large amounts of desert dust in the troposphere, resulting in enhanced optical thickness that is correlated with the aerosol direct radiative forcing.

Dust aerosols have a significant direct impact on the earth's radiation budget, by attenuating the outgoing

longwave (LW) radiation and reducing the solar flux available to heat the surface. Dust aerosols reflect sunlight back into space, and are known to influence cloud formation and precipitation.

To assess the aerosol effect of desert dust, this study describes a new algorithm to retrieve the aerosol optical depth (AOD) over the desert using the Spinning Enhanced Visible and Infrared Imager (SEVIRI) window channels. SEVIRI is on board the Meteosat Second Generation (Schmetz et al. 2002) and provides imagery products in 12 spectral bands, 3 of which are in the window region of the atmospheric absorption of the thermal spectrum.

The Sahara is the largest desert on the earth and it covers a large area in the middle of the field of view of Meteosat, which makes this satellite particularly

---

*Corresponding author address:* Bart De Paepe, Royal Meteorological Institute of Belgium, Ringlaan 3, 1180 Brussels, Belgium.  
E-mail: bart.depaepe@oma.be

interesting for studying dust aerosols. Additionally, its temporal resolution of 15 min allows the aerosols to be monitored continuously in time and space. Until now desert regions often appeared as a gap on the current aerosol retrievals, since most aerosol retrieval algorithms use the solar channels that are not suited to work over bright reflecting surfaces, such as the desert. Algorithms that use other parts of the spectrum, such as the ultraviolet (Hsu et al. 2004), help to overcome these problems. In addition to the spectral information, there are algorithms that use angular information to retrieve the aerosol optical properties. The Multiangle Imaging Spectroradiometer (MISR) instrument (Diner et al. 1998) observes the atmosphere and the aerosols over a wide range of different angles to retrieve the AOD.

The LW radiation measured by the satellite is composed of both the surface radiation and the radiation emitted by the atmosphere. Therefore, if we want to retrieve aerosol information from the atmospheric radiation, we have to account first for the surface radiation. This can be done using the thermal contrast method (King et al. 1999), under the assumption that the surface contribution remains constant over the course of several days that are used to obtain the clear-sky values. This is required because the surface radiation is directly related to the surface temperature. Additionally the clear-sky values, as well as the instantaneous measurements, need to be corrected for the emission and absorption by the atmosphere. Next, we discuss the AOD retrieval algorithm, which concerns the simulations and the inversion. Finally, we apply the aerosol retrieval to a small dust event from 19 to 22 June, and validate our results with the Cloud Aerosol lidar and Infrared Pathfinder Satellite Observations (CALIPSO) AOD.

## 2. Atmospheric correction

The LW radiation measured by the satellite has been modified during its passage through the atmosphere. The atmosphere is characterized by the presence of several gases that absorb and emit radiation. The absorption and emission depend on the type of the gas, and additionally the emission depends on the temperature profile of the atmosphere. To retrieve information on the surface radiation in the different SEVIRI thermal infrared (IR) channels, but also on the aerosol content, the measured radiation in each channel and for every observation needs to be corrected for the atmospheric gases contribution to the radiation.

The atmospheric correction of a satellite observation requires the corresponding atmospheric profile of temperature, water vapor (the most important gaseous absorber in the thermal IR) (Schmetz and Turpeinen 1988),

and additionally ozone, carbon dioxide, oxygen, nitrous oxide, and methane. Applying the radiative transfer equation to this profile allows us to calculate the atmospheric radiation. In the thermal IR we can assume that there is no scattering by the atmospheric gases, therefore we can apply the Schwarzschild equation:

$$\mu \frac{dL_\lambda}{d\tau_\lambda} = -L_\lambda(\theta, \phi) + B_\lambda(T), \quad (1)$$

where  $\mu$  is the cosine of the view zenith angle,  $L_\lambda$  is the incoming radiation at wavelength  $\lambda$  in the direction of the solid angle defined by the view zenith angle ( $\theta$ ) and the azimuthal angle ( $\phi$ ),  $\tau$  is the optical depth, and  $B(T)$  is the Planck radiation that corresponds to the temperature  $T$ . Schmetz (1986) provided a practical solution to calculate the emission and absorption of LW radiation in the atmosphere. The atmosphere is divided into several horizontal levels corresponding to a vertical atmospheric profile. The Schwarzschild equation is integrated over the consecutive atmospheric levels and the resulting radiance serves as input for the following layer, defined between an upper and lower level. The temperature, water vapor, and ozone amount for each layer are derived from the surrounding level values. To apply this solution to the SEVIRI window channels we implemented the Streamer (Key 2001) code for the absorption by the atmospheric gases. Streamer accounts for four gases: water vapor, ozone, carbon dioxide, and oxygen; where the latter two are derived from the atmospheric temperature profile. To cover the entire spectral interval of a SEVIRI channel, we combine several Streamer bands and attribute a weight to them, according to their spectral response as shown in Table 1 (M. Doutriaux-Boucher 2006, personal communication).

At 8.7 and 10.8  $\mu\text{m}$  only the absorption amounts of water vapor and ozone are present, at 12.0  $\mu\text{m}$  only those of water vapor and carbon dioxide. The absorption amounts of these gases are determined with the exponential-sum fitting of transmissions (ESFT) technique (Wiscombe and Evans 1977), which parameterizes the many absorption lines that may exist in a given spectral region. The atmospheric profiles of temperature, water vapor, and ozone were obtained from the European Centre for Medium-Range Weather Forecasts (ECMWF) archive on a  $0.5^\circ \times 0.5^\circ$  grid over the region of interest at 0000, 0600, 1200, and 1800 UTC. For these data the atmospheric radiation is calculated for every absorption line of every single gaseous component, for all gases, and for all bands needed to cover the wavelength interval of the SEVIRI channel. To correct an observation for the atmospheric contamination, we select the closest grid point

TABLE 1. Streamer bands used to characterize the SEVIRI window channels' spectral response functions.

SEVIRI channel	IR087	IR108	IR120
SEVIRI IR channel No.	3	5	6
Streamer channel	8	10	11
Streamer start band	55	43	39
Streamer end band	59	49	44
Bandweight <sub><i>i</i></sub>	0.0468	0.0843	0.0442
Bandweight <sub><i>i</i>+1</sub>	0.7404	0.6695	0.62952
Bandweight <sub><i>i</i>+2</sub>	0.8468	0.8765	0.9445
Bandweight <sub><i>i</i>+3</sub>	0.5928	0.9132	0.9787
Bandweight <sub><i>i</i>+4</sub>	0.0449	0.9805	0.6074
Bandweight <sub><i>i</i>+5</sub>		0.6288	0.0190
Bandweight <sub><i>i</i>+6</sub>		0.0378	

to every pixel and the smallest time span between the observation and the archive.

For the retrieval of the surface properties (section 3) we also need the radiation at 3.9  $\mu\text{m}$ . During daytime, this channel has both thermal and solar contribution. Therefore, we cannot use the solution by Schmetz. However, Kratz (2005) developed a very similar algorithm, that accounts also for the incoming solar radiation at the 3.9- $\mu\text{m}$  channel. We adopted his code for the SEVIRI 3.9- $\mu\text{m}$  channel to allow computation of the upward and downward atmospheric radiation at 3.9  $\mu\text{m}$ . The correlated  $k$ -distribution method (Kratz 1995) is used to determine the atmospheric absorption and emission attributed to water vapor, carbon dioxide, methane, and nitrous oxide, where  $k$  is the absorption coefficient. Then the atmospheric radiation is calculated for every  $k$  of the gaseous component, for all gases and for the entire SEVIRI 3.9- $\mu\text{m}$  channel interval.

The transmitted radiation in the 10- $\mu\text{m}$  window channels and in the 3.5- $\mu\text{m}$  window is calculated also using Schmetz and Kratz, respectively, except that we account only for absorption, and not for emission in the Schwarzschild equation. Then the transmittance corresponds to the ratio of the outgoing radiation at the top of the atmospheric profile and the ingoing radiation at the bottom of the profiles.

### 3. Surface contribution

The surface radiation depends on the surface temperature and on the surface emissivity. We calculate these properties for the window channels using the satellite observations. First, we make sure that the radiation comes from the surface, and not from other features such as clouds or aerosols. All these features have their own spectral signature in terms of the radiation that is emitted.

Legrand et al. (2001) showed that LW radiation reaching the satellite decreases in the presence of aerosols and clouds, except at night, when the LW radiation can

increase in the presence of aerosols. Therefore, we approximate the clear-sky radiation for the day and time of our interest by taking the maximum radiation at 10.8  $\mu\text{m}$ , which is the clearest window channel, over a 30-day span centered around this day and for the same time of the day. Additionally we test if the brightness temperature (BT) difference between the channels at 8.7 and 10.8  $\mu\text{m}$  falls within 3 K of the most negative difference observed so far. The clear-sky desert surface is characterized by small emissivity at 8.7  $\mu\text{m}$  and as a consequence the clear-sky desert surface radiation at 8.7  $\mu\text{m}$  is low. Zhang et al. (2006) used this characteristic to distinguish dust storms ( $\text{BT}_{8.7} - \text{BT}_{10.8} \geq 0$ ) from the clear-sky desert surface ( $\text{BT}_{8.7} - \text{BT}_{10.8} \ll 0$ ). We assume that within 30 days every satellite pixel is cloud and aerosol free for at least one observation. The clear-sky values for the other window channels are taken at the same observation time.

Hence, we obtain a composite image that represents the top-of-the-atmosphere (TOA) clear-sky radiation ( $L_{\text{cs}\Delta\lambda}$ ). This image needs to be corrected for the atmospheric radiation ( $L_{\text{atm}\Delta\lambda}$ ; as described in section 2) to obtain the apparent surface clear-sky radiation ( $L_{\text{scs}\Delta\lambda}$ ). We use the equation for the atmospheric transmittance ( $t_{\text{atm}\Delta\lambda}$ ) to calculate the  $L_{\text{scs}\Delta\lambda}$ :

$$L_{\text{scs}\Delta\lambda} = \frac{L_{\text{cs}\Delta\lambda} - L_{\text{atm}\Delta\lambda}}{t_{\text{atm}\Delta\lambda}}. \quad (2)$$

Since the transmittance only accounts for atmospheric absorption, we must subtract the amount of radiation emitted by the atmosphere from the  $L_{\text{cs}\Delta\lambda}$ .

The surface emissivity and temperature are derived using a method described by Minnis et al. (2002), which is based upon previous work by Becker and Li (1990) and Li and Becker (1993).

- At nighttime the surface emissivity for the 10- $\mu\text{m}$  window channels as well as at the 3.5- $\mu\text{m}$  window can be obtained by

$$\epsilon_{\Delta\lambda} = \frac{[B_{\Delta\lambda}(T_{\text{s}\Delta\lambda}) - L_{\text{a}\Delta\lambda}]}{[B_{\Delta\lambda}(T_{\text{skin}}) - L_{\text{a}\Delta\lambda}]}, \quad (3)$$

where  $L_{\text{a}\Delta\lambda}$  is the downwelling atmospheric radiation,  $B_{\Delta\lambda}(T_{\text{skin}})$  is the Planck surface radiation,  $B_{\Delta\lambda}(T_{\text{s}\Delta\lambda})$  is the apparent surface radiation, and  $\epsilon_{\Delta\lambda}$  represents the surface emissivity.

- If we assume that over desert  $L_{\text{a}\Delta\lambda} \ll B_{\Delta\lambda}(T_{\text{skin}})$  (Ackerman 1997), then this equation becomes

$$\epsilon_{\Delta\lambda} = \frac{[B_{\Delta\lambda}(T_{\text{s}\Delta\lambda})]}{[B_{\Delta\lambda}(T_{\text{skin}})]} \quad (4)$$

and at 10.8  $\mu\text{m}$

$$\epsilon_{10.8} = \frac{[B_{10.8}(T_{s10.8})]}{[B_{10.8}(T_{\text{skin}})]}. \quad (5)$$

- From this we can solve  $T_{\text{skin}}$ :

$$T_{\text{skin}} = \left[ \frac{B_{10.8}(T_{s10.8})}{m_{10.8}\epsilon_{10.8}} \right] \frac{1}{n_{10.8}}, \quad (6)$$

where the coefficients  $m_{\Delta\lambda}$  and  $n_{\Delta\lambda}$  are given by the power-law approximation (Jiang et al. 2006):

$$B_{\Delta\lambda}(T) = m_{\Delta\lambda} T^{n_{\Delta\lambda}}. \quad (7)$$

- Then we can define an emissivity ratio:

$$\epsilon'_{\Delta\lambda} = \frac{\epsilon_{\Delta\lambda 1}}{\epsilon_{\Delta\lambda 2}} = \frac{[B_{\Delta\lambda 1}(T_{s\Delta\lambda 1})]}{[B_{\Delta\lambda 1}(T_{s\Delta\lambda 2})]} \quad (8)$$

and at 3.9  $\mu\text{m}$

$$\epsilon'_{3.9} = \frac{\epsilon_{3.9}}{\epsilon_{10.8}^{n_{10.8}}} = \frac{[B_{3.9}(T_{s3.9})]}{[B_{3.9}(T_{s10.8})]}. \quad (9)$$

- At ground level the radiance at 3.9  $\mu\text{m}$  during daytime can be written as

$$B_{3.9}(T_{s3.9}) = \epsilon_{3.9}[B_{3.9}(T_{\text{skin}})] + \alpha_{3.9}[\chi S_{3.9} + L_{\alpha 3.9}], \quad (10)$$

where  $S_{3.9}$  represents the solar contribution that we approximate by the solar constant at the TOA:  $4.92/(\text{earth-sun distance})^2 [\text{m W m}^{-2} \text{sr}^{-1} (\text{cm}^{-1})^{-1}]$  [from the European Organisation for the Exploitation of Meteorological Satellites (EUMETSAT); Rosenfeld 2005], which is corrected for the atmospheric extinction and the solar zenith angle.

The  $\chi$  is the anisotropic correction factor [we used the Clouds and the Earth's Radiant Energy System/Tropical Rainfall Measuring Mission (CERES/TRMM) shortwave ADMs for clear-sky land and desert available online at <http://asd-www.larc.nasa.gov/Inversion/adm/adm.html>; Loeb et al. 2003], and  $\alpha = 1 - \epsilon$  represents the surface albedo.

- Rearranging this equation to resolve  $\epsilon_{3.9}$ , neglecting  $L_{\alpha 3.9}$ , and substituting  $\epsilon_{3.9}$  in the first term by the emissivity ratio and  $T_{\text{skin}}$  by the apparent surface temperature at 10.8  $\mu\text{m}$  allows us to calculate the emissivity at 3.9  $\mu\text{m}$

$$\epsilon_{3.9} \approx 1 - \frac{\{B_{3.9}(T_{s3.9}) - \epsilon'_{3.9}[B_{3.9}(T_{s10.8})]\}}{\chi S_{3.9}}. \quad (11)$$

Once we know  $\epsilon_{3.9}$ , which we assume to be constant over 24 h (Faysash and Smith 1999), we can calculate the surface temperature using nighttime data. Finally, we compute the emissivity at 8.7, 10.8, and 12.0  $\mu\text{m}$  using the nighttime radiances using Eq. (4). The result is illustrated for 19 June 2007 in Fig. 1.

For most of the pixels we obtained a surface emissivity at 3.9  $\mu\text{m}$  in Fig. 1a, which is lower compared to the values for desert surface reported by Minnis et al. (2002) and Peres and DaCamara (2005). The emissivities at 8.7, 10.8, and at 12.0  $\mu\text{m}$ , on the other hand, agree well with the reported values listed in Table 2. The last row of this table shows the retrieved emissivities without neglecting  $L_{\alpha\Delta\lambda}$  in Eq. (3). We find that the resulting emissivities at 3.9 and at 8.7  $\mu\text{m}$  are significantly smaller than those reported by Minnis et al. (2002) and Peres and DaCamara (2005). The deterioration of the retrieved surface emissivity is due to the inaccuracy of the estimated downward atmospheric radiation, which is very sensitive to the temperature profile of the lower atmosphere. Therefore, we decided to ignore it for the aerosol retrievals.

#### 4. Aerosol retrieval

We retrieve the AOD by inversion of the thermal IR satellite signal. The LW radiation measured by the satellite is composed of the surface radiation and the radiation emitted by the atmosphere. Therefore, if we want to retrieve aerosol information from the atmospheric radiation, we have to account first for the surface radiation as discussed in section 3. The resulting clear-sky image was obtained assuming that the radiance emitted by the surface is constant over the time of observation (King et al. 1999).

Typically, over the desert dust storms are triggered by strong winds coming from the north that easily drop the surface temperature by 10° (Slingo et al. 2006). Nevertheless this dust impacts the downwelling radiative fluxes at the surface (Vergé-Dépré et al. 2006), the observed radiances will also depend on the changes of the surface and of the atmospheric temperature that are induced by the change of the aerosol loading, instead of on the change of the aerosol loading itself.

To address this problem there are two possibilities: the first one is to accurately define the temperature of the entire surface-atmosphere system and the second one is to bypass the impact of the temperature.

We choose the latter option. The surface radiation is also a function of the surface emissivity, which is constant for a given surface type according to Eq. (4). The desert surface is characterized by very low emissivity at 8.7  $\mu\text{m}$  (mean value of 0.78) against mean



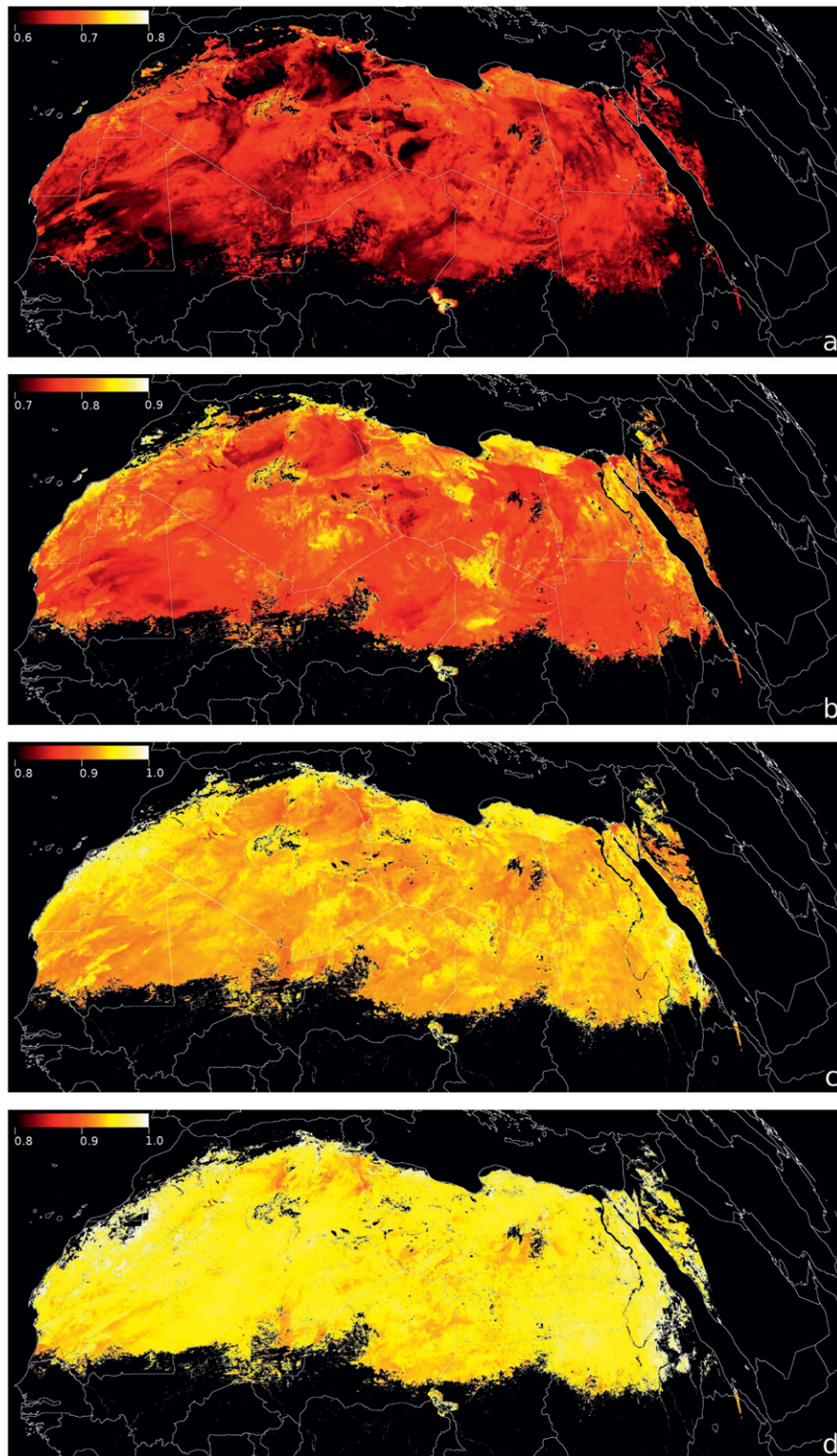


FIG. 1. Surface emissivity at (a) 3.9, (b) 8.7, (c) 10.8, and (d) 12.0  $\mu\text{m}$  for 19 Jun 2007.

TABLE 2. The mean surface emissivity and the std dev.

	3.9 $\mu\text{m}$	8.7 $\mu\text{m}$	10.8 $\mu\text{m}$	12.0 $\mu\text{m}$
19 Jun 2007	0.704 (0.058)	0.784 (0.049)	0.930 (0.013)	0.950 (0.014)
Minnis	0.758 (0.053)	0.757 (0.080)	0.934 (0.010)	0.963 (0.013)
Peres	0.766 (0.252)	0.821 (0.347)	0.948 (0.020)	0.966 (0.016)
19 Jun 2007 accounting for $L_{a\Delta\lambda}$	0.660 (0.076)	0.718 (0.073)	0.924 (0.02)	0.954 (0.022)

values of 0.93 and 0.95 at 10.8 and at 12.0  $\mu\text{m}$ , respectively (see Table 2). As a result the desert surface radiation at 8.7  $\mu\text{m}$  is much smaller than that at 10.8 and at 12.0  $\mu\text{m}$ . In the presence of aerosols, the observed radiances at 8.7, 10.8, and 12.0  $\mu\text{m}$  lie closer together, suggesting that the corresponding emissivities of the aerosol layer converge. This would allow us to relate the difference between the surface emissivity and the aerosol layer emissivity to AOD. But the standard methods to compute surface emissivities (Peres and DaCamara 2005; Faysash and Smith 1999; Jiang et al. 2006; Peres and DaCamara 2004) require two observations at two different temperatures, typically one during daytime and another during nighttime, of the same scene. Therefore, it is impossible to calculate the emissivity of an aerosol layer that typically changes over time and space. Instead we eliminate the skin temperature from the emissivity [Eq. (4)] at two wavelengths  $\Delta\lambda_1$  and  $\Delta\lambda_2$ . Thus, we use the emissivity ratio [Eq. (8)].

In this way we define  $\epsilon'_{8.7_{10.8}} = [B_{8.7}(T_{s8.7})]/[B_{8.7}(T_{s10.8})]$  and  $\epsilon'_{8.7_{12.0}} = [B_{8.7}(T_{s8.7})]/[B_{8.7}(T_{s12.0})]$ . In agreement with the low desert surface emissivity at 8.7  $\mu\text{m}$  we find low values for clear-sky simulations for both emissivity ratios that increase for increasing AOD. This is illustrated in Fig. 2. The relation between AOD and emissivity ratio depends on the surface temperature and on the atmospheric temperature profile (accounted for by the aerosol layer temperature), due to the wavelength dependence of the absorption and emission by the aerosol layer. But, for every AOD there are exactly one  $\epsilon'_{8.7_{10.8}}$  and one  $\epsilon'_{8.7_{12.0}}$  that have the same surface temperature and atmospheric temperature. For different surface emissivities the graphs will shift along the y axis according to Eq. (8).

This allows us to retrieve the AOD by inversion of the observed emissivity ratios without knowing any value of the surface temperature and of the atmospheric temperature profile. The best combined match of the observed  $\epsilon'_{8.7_{10.8}}$  and  $\epsilon'_{8.7_{12.0}}$  together, which imperatively must have the same surface temperature and atmospheric temperature, results in the corresponding AOD. At another AOD the relation between  $\epsilon'_{8.7_{10.8}}$  and  $\epsilon'_{8.7_{12.0}}$  for the same temperatures would be modified.

## 5. Simulations

We retrieve the AOD by combined inversion of the emissivity ratios  $\epsilon'_{8.7_{10.8}}$  and  $\epsilon'_{8.7_{12.0}}$ . Therefore, at each SEVIRI thermal IR wavelength we independently simulate the radiation for different values of AOD, according to the vertical distribution of the particle loading, aerosol layer temperature, and for several values of surface emissivity and surface temperature to account for the surface variability. The aerosol layer temperature replaces the dependence on the atmospheric temperature profile. The simulated radiances at 8.7 and 10.8  $\mu\text{m}$ , and at 8.7 and 12.0  $\mu\text{m}$  are then used to calculate  $\epsilon'_{8.7_{10.8}}$  and  $\epsilon'_{8.7_{12.0}}$ , respectively. Figure 2 shows the results for simulations considering fixed surface emissivities of 0.78, 0.93, and 0.95 at 8.7, 10.8, and 12.0  $\mu\text{m}$ , respectively, for 7 values of surface temperature between 288 and 318 K with a 5-K increment, and for 2 values of aerosol layer temperature at 230 and 270 K, and for 27 values of AOD as specified later in this section.

We selected the Optical Properties of Aerosols and Clouds (OPAC; Hess et al. 1998) package's desert aerosol model for the optical properties, defined by the extinction coefficient, the single-scattering albedo, and the asymmetry parameter. We calculated the AOD ( $\tau$ ) for these properties and for different values of the particle number density [ $N_j(0)$ ]:

$$\tau = \sum_j \sigma_{e,j}^1 N_j(0) \int_{H_{j,\min}}^{H_{j,\max}} e^{-z_j/h} dh,$$

where  $j$  is the index of the atmospheric layer;  $\sigma_e^1$  is the extinction coefficient normalized to a number density of 1 particle  $\text{cm}^{-3}$ ;  $H_{j,\min}$  and  $H_{j,\max}$  are the height of the lower and upper boundary of this layer, respectively;  $h$  denotes the height; and  $z_j$  is the scale height. The scale height informs on the distribution of the particles in the layer. The OPAC desert aerosol model distinguishes an aerosol layer, troposphere, and stratosphere with a particle number density of 2300, 730, and 3 particles  $\text{cm}^{-3}$  at the surface level, respectively. The aerosol layer lies between 0 and 6 km, the troposphere between 0 and 12 km, and the stratosphere above 12 km. The troposphere and the stratosphere have a fixed scale height of

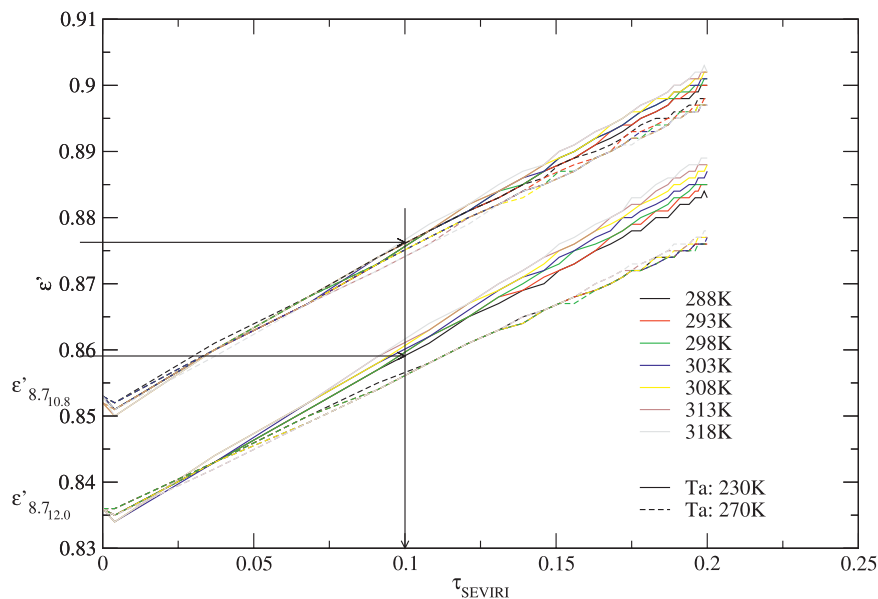


FIG. 2. Here  $\tau_{\text{SEVIRI}}$  against  $\epsilon'_{8.7,10.8}$  and  $\epsilon'_{8.7,12.0}$ . The emissivity ratios are calculated from simulations using several surface temperatures (corresponding to the different colors) and two different aerosol layer temperatures (corresponding to the dashed and solid lines), but for a constant surface emissivity depending on the wavelength.

8 and 99 km, respectively, but in the aerosol layer the scale height can vary from 1 (heterogeneous aerosol layer where the particle number density decreases rapidly with increasing altitude) to 99 km (homogeneous aerosol layer where the particle number density is constant from bottom to top). We vary the AOD by changing the scale height of the aerosol layer. The resulting AOD can be seen in Fig. 3. Note that the AOD for the high aerosol layer scale heights is approximately between 0.24 and 0.31 depending on the wavelength. This is much smaller than the AOD for the solar channels, which is typically around 0.5 in the presence of dust aerosols (Husar et al. 1997). For the simulations of the radiance in the presence of aerosols we selected several scale heights (Table 3) for the aerosol layer to obtain the entire range of AODs as shown on Fig. 3.

We simulated the radiance through the aerosol layer using the two-stream approximation (Ackerman 1997) for the three thermal IR wavelengths independently for 27 AODs (including the case without an aerosol layer, but still with aerosols in the troposphere and the stratosphere; and the case where  $\text{AOD} = 0$ ), for 58 values of surface temperature, for 20 values of surface emissivity, and for 9 aerosol layer temperatures, as specified in Table 3, and stored the simulated radiances in lookup tables (LUTs).

From these simulated radiances we compute emissivity ratios. Note that the simulations do not account for atmospheric emission, extinction, or the presence of

clouds. As a consequence, the satellite observations from which we want to retrieve the aerosol information have to be corrected for this atmospheric gases contribution, and have to be cloud free.

## 6. Retrieval algorithm

To retrieve the SEVIRI AOD at  $8.7 \mu\text{m}$ , further referred to as  $\tau_{\text{SEVIRI}}$ , we need the three instantaneous thermal IR observations as well as the corresponding clear-sky images for the same time of observation as described in section 3. These data need to be corrected for the atmospheric radiation as shown in section 2. These corrected data are input to calculate the emissivity ratios, both the instantaneous and the clear sky as discussed in section 4. To obtain the surface emissivity we assume that the surface contribution remains constant over 30 days. As a consequence, the retrieved surface emissivity is assumed to be constant over 30 days as well. Then as illustrated in Fig. 4, for each pixel we subsample the LUT, which was simulated as described in section 5, only maintaining the simulations that correspond to the observed emissivities  $\pm 0.01$  in all three channels independently. The remaining part of the LUT is then used to match the emissivity ratios for  $\tau = 0$ , that corresponds to the clear sky, with the observed clear-sky emissivity ratio, for both  $\epsilon'_{8.7,10.8}$  and  $\epsilon'_{8.7,12.0}$  independently. This results in a set of simulated emissivity ratios that are only a function of the aerosol layer

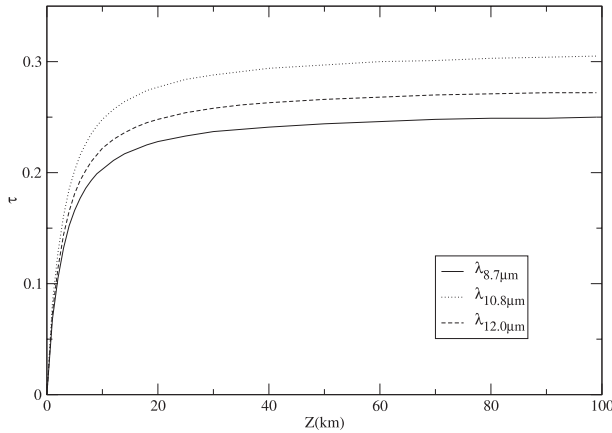


FIG. 3. AOD ( $\tau$ ) simulations at 8.7, 10.8, and 12.0  $\mu\text{m}$  as a function of scale height  $Z$  for the OPAC desert aerosol model with an exponential particle number density distribution between 0 and 16 km (the aerosol layer between 0 and 6 km, superposed by the troposphere from 6 to 12 km, and the stratosphere beyond 12 km). The surface particle number of the aerosol layer = 2300 particles  $\text{cm}^{-3}$ , the troposphere = 730 particles  $\text{cm}^{-3}$ , and the stratosphere = 3 particles  $\text{cm}^{-3}$ .

temperature, the surface temperature, and  $\tau$ . Then, we match this set with the observed instantaneous emissivity ratios to find the best match between the observed  $\epsilon'_{8.7,10.8}$  and the simulated  $\epsilon'_{8.7,10.8}$  on one side, and between the observed  $\epsilon'_{8.7,12.0}$  and the simulated  $\epsilon'_{8.7,12.0}$  on the other side, which imperatively must have the same aerosol and surface temperature. The best match is associated with a certain value of  $\tau$  that is scaled according to the relation between the observed  $\epsilon'_{8.7,10.8}$  and the simulated  $\epsilon'_{8.7,10.8}$ , and between the observed  $\epsilon'_{8.7,12.0}$  and the simulated  $\epsilon'_{8.7,12.0}$ .

**7. Results**

We implemented our new algorithm on nighttime and daytime observations between 19 and 22 June 2007. During this period there was a small dust storm over the Sahara that was observed by CALIPSO (operational since July 2006). Figures 5–8 correspond to all the CALIPSO overpasses over the Sahara during this period. The region of our interest is defined by 34°N to the north, 10°N to the south, 18°W to the west, and 40°E to the east, which covers the entire Sahara.

Figures 5a,e plot  $\tau_{\text{SEVIRI}}$  and  $\tau_{\text{CALIPSO}}$  on the  $y$  axis against the CALIPSO track ( $x$  axis) at 0030 UTC and at 0215 UTC 19 June 2007. The  $\tau_{\text{SEVIRI}}$ , masked by the Meteorological Product Extraction Facility (MPEF) cloud screening, were averaged over  $3 \times 3$  SEVIRI pixels to completely cover the CALIPSO pixel that has a 5-km horizontal resolution. The  $y$  axis on the left side is for  $\tau_{\text{SEVIRI}}$ , the right side is for  $\tau_{\text{CALIPSO}}$ . Figures 5b and 5f show  $\tau_{\text{SEVIRI}}$  over the Sahara with the MPEF cloud mask (CM; Lutz 1999) on the same time of observation as in Figs. 5a and 5e, respectively. The Sahara region on the SEVIRI images is defined by the U.S. Geological Survey Global Land Cover Characterization (see online at <http://edc2.usgs.gov/glcc/>). The gray pixels are not part of the Sahara nor do they correspond to clouds. The location of the CALIPSO track is indicated by a black line with the indication of latitude and longitude coordinates along the line. The MPEF cloud screening is based on a multispectral threshold technique described in Lutz (1999). The first two tests compare SEVIRI reflectances in individual bands and their differences with thresholds. The next two tests compare threshold brightness temperatures and their differences, respectively. The fifth test is a threshold on standard deviation of both solar and thermal channels. Two final tests on sun glint and on snow and ice complete the scene identification algorithm.

The MPEF CM is disseminated in near-real time and can also be obtained from the EUMETSAT Unified Meteorological Archive and Retrieval Facility. Please note that ongoing improvements in the MPEF CM algorithm (Lutz 1999) do not trigger reprocessing of the archive. As a result, the EUMETSAT data used in this study reflect the status of the MPEF CM effective as of 2007. Inaccurate cloud screening can result in a bad retrieval of the aerosol optical properties. We illustrate this by applying the MPEF CM to our results. Figures 5d and 5h show  $\tau_{\text{SEVIRI}}$  over the Sahara without the MPEF cloud screening on the same times of observation as Figs. 5b and 5f, respectively. Figures 5c and 5g show the dust red–green–blue (RGB) composite image (defined by 12.0 – 10.8, 10.8 – 8.7, and 10.8  $\mu\text{m}$ ), over the same region and for the same time of observation as Figs. 5b and 5f, respectively. The dust can be identified as the

TABLE 3. The simulation parameters.

Scale height (km)	1, 2, 3, 4, 5, 6, 7, 8, 9, 10, 12, 14, 16, 18, 20, 25, 30, 35, 40, 50, 60, 70, 80, 90, 99
$\epsilon_{8.7}$	From 0.67 to 0.86, with 0.01 increments
$\epsilon_{10.8}$ and $\epsilon_{12.0}$	From 0.80 to 0.99, with 0.01 increments
Surface temperature	From 283 to 340 K, with 1-K increments
Aerosol layer temperature	From 230 to 270 K, with 5-K increments



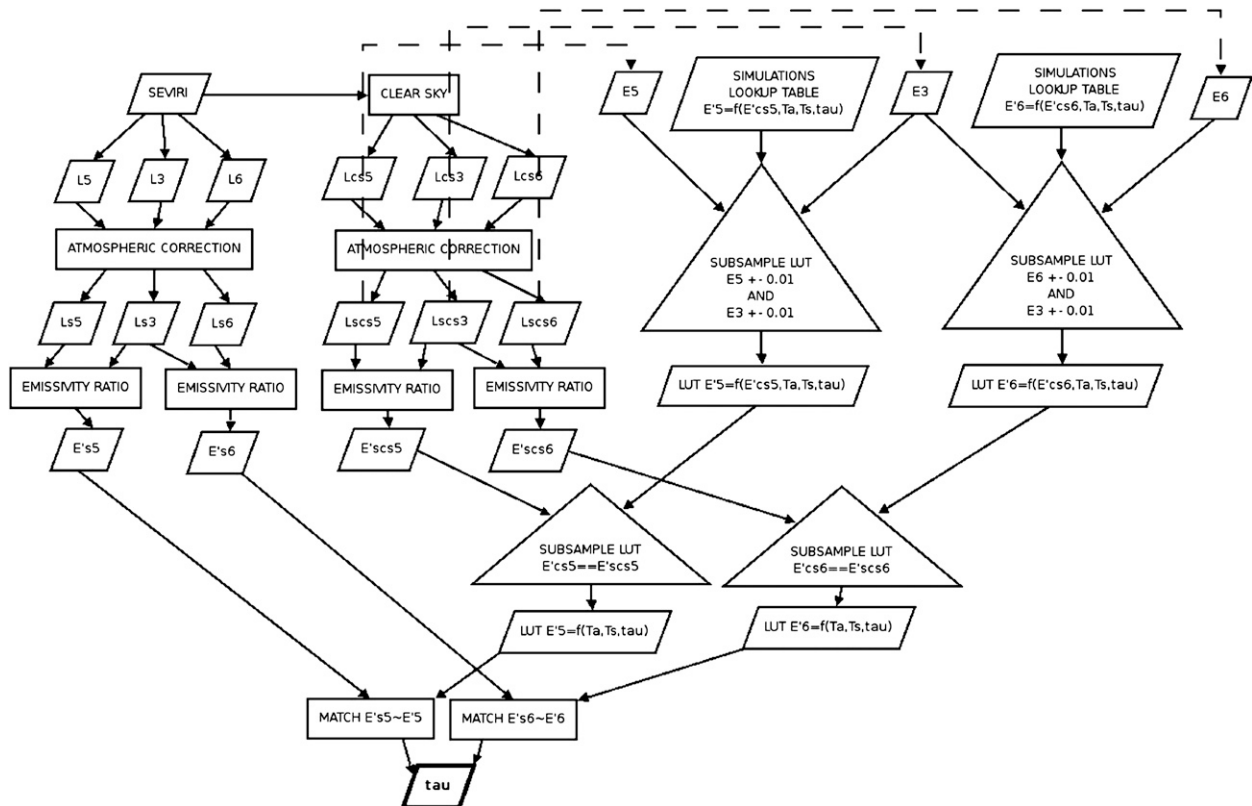


FIG. 4. Flowchart of the aerosol retrieval algorithm. Numbers correspond to the SEVIRI IR channel corresponding to Table 1. Here  $L$  is radiance,  $L_s$  is apparent surface radiance,  $L_{cs}$  is clear-sky radiance,  $L_{scs}$  is clear-sky apparent surface radiance,  $E$  is surface emissivity,  $E'$  is emissivity ratio,  $E'_{cs}$  is clear-sky emissivity ratio,  $E'_{scs}$  is clear-sky apparent surface emissivity ratio,  $T_a$  is aerosol layer temperature,  $T_s$  is surface temperature, and  $\tau$  is AOD.

pink areas on the dust RGB. This is the recommended RGB for monitoring of dust storms during both day and night (Kerkmann 2004). Apart from the dusty regions, this RGB allows us to detect low clouds (dark blue) and high clouds (green to red). Figures 6, 7, and 8 show the same image sequence at 1300 UTC 19 June 2007, 0115 and 1345 UTC 20 June 2007, 0200 UTC 21 June 2007, and 0115 and 0245 UTC 22 June 2007.

## 8. Discussion and validation

In this section we compare the  $\tau_{SEVIRI}$  retrievals with the CALIPSO AOD ( $\tau_{CALIPSO}$ ). The CALIPSO satellite provides atmospheric profiles that allow us to analyze the vertical structure of clouds and aerosols, as well as their overlap. Therefore CALIPSO disposes of an active lidar instrument, the Cloud-Aerosol Lidar with Orthogonal Polarization (CALIOP; Winker et al. 2004). The CALIPSO data products are available as single files in HDF format from the Langley Atmospheric Science Data Center. For this study we used the lidar level 2 aerosol layer products, version 2.01, with a 5-km hori-

zontal resolution. The aerosol layer products provide feature optical depth at 532 nm (Vaughan et al. 2004). Comparison is the only kind of validation we can do at this moment, because no other IR AOD product over the desert is available from satellite instruments or from ground-based measurements.

In the case of CALIPSO the validation of the algorithm was limited to SEVIRI pixels along the CALIPSO satellite track as indicated in section 7.

Figures 5 to 8 are presented chronologically, with each figure containing two consecutive cases.

Figure 5a shows low  $\tau_{SEVIRI}$  and  $\tau_{CALIPSO}$  along the track as there is no dust aerosol as can be seen in Fig. 5c. Except around  $14^\circ\text{N}$  where  $\tau_{SEVIRI}$  increases as the track passes along the east of the Bodele Depression, that is known to be a source region of dust aerosols. However,  $\tau_{CALIPSO}$  does not increase at this place.

In Fig. 5e both  $\tau_{SEVIRI}$  and  $\tau_{CALIPSO}$  are characterized by high AOD around  $19.1^\circ\text{N}$ . In Fig. 5g we observe that this area is covered by a cloudy band, which is responsible for the increased AOD that spreads from Senegal to Ethiopia.

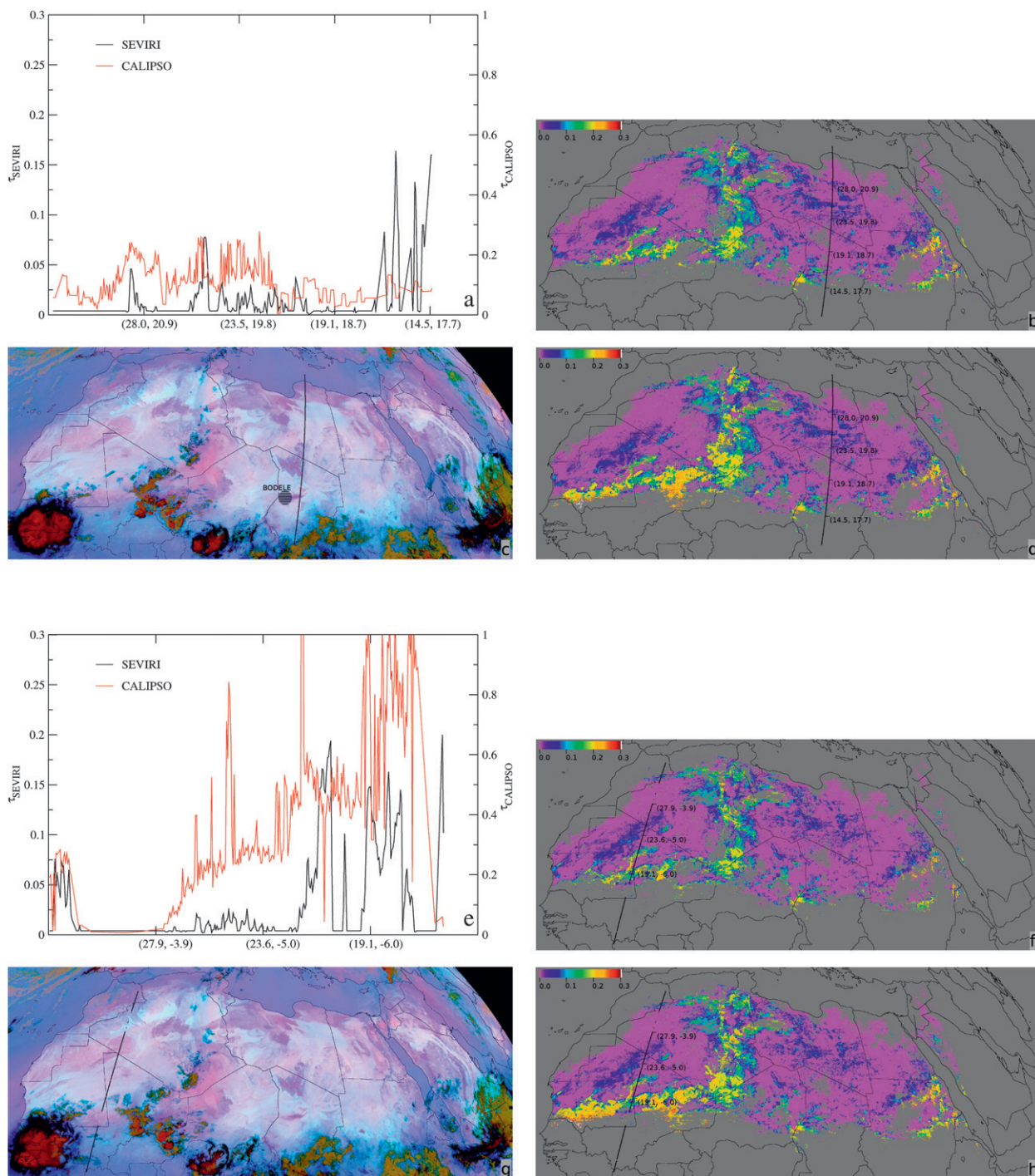


FIG. 5.  $\tau_{SEVIRI}$  and  $\tau_{CALIPSO}$  along the CALIPSO track at (a) 0030 and (e) 0215 UTC 19 Jun 2007.  $\tau_{SEVIRI}$  (b),(f) with and (d),(h) without the MPEF CM, with the indication of the CALIPSO track. (c),(g) The dust RGB with the indication of the CALIPSO track. Latitude and longitude coordinates are indicated along the CALIPSO track in the images, and along the  $x$  axis in the graphs.

Figure 6c detects a dust storm corresponding to the pink plume over Mali, Niger, and Algeria. The CALIPSO track crosses the dust plume around 19.1°N corresponding to the SEVIRI peak in Fig. 6a. On the other hand, CALIPSO does not retrieve increased AOD at

this place, which is probably due to differences in the cloud screening between SEVIRI and CALIPSO. For this case the SEVIRI peak corresponds to the center of the pink region in Fig. 6c, suggesting that the CALIPSO cloud screening masked the dust aerosols as cloud. To



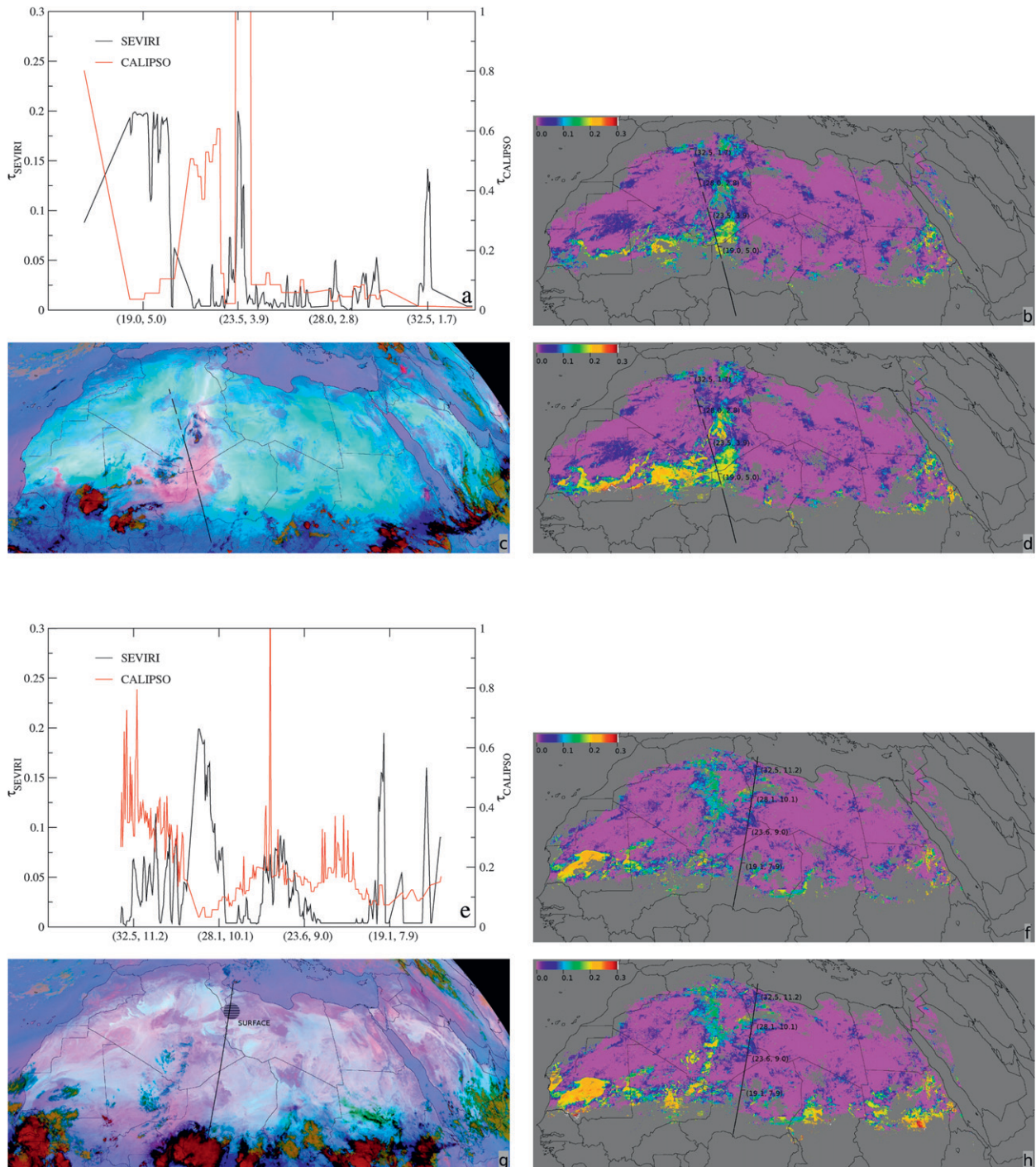


FIG. 6. As in Fig. 5, but for  $\tau_{\text{SEVIRI}}$  and  $\tau_{\text{CALIPSO}}$  along the CALIPSO track at (a) 1300 UTC 19 Jun 2007 and (e) 0115 UTC 20 Jun 2007.

the north, between  $19.1^{\circ}$  and  $23.6^{\circ}\text{N}$ , the SEVIRI image is contaminated by the presence of small clouds. In Fig. 6a  $\tau_{\text{SEVIRI}}$  and  $\tau_{\text{CALIPSO}}$  retrieve exactly the reverse AOD for this interval, which is due to the different cloud screening. However, both  $\tau_{\text{SEVIRI}}$  and  $\tau_{\text{CALIPSO}}$  are characterized by a peak at  $23.6^{\circ}\text{N}$  that correspond to

a cloud in Fig. 6c. Around  $32.5^{\circ}\text{N}$ ,  $\tau_{\text{SEVIRI}}$  is characterized by another peak, that now is probably due to the surface properties.

In Fig. 6e, 12 h later, the dust plume disappeared and the CALIPSO track crosses the clear-sky desert surface. Nevertheless, Fig. 6e is characterized by several peaks

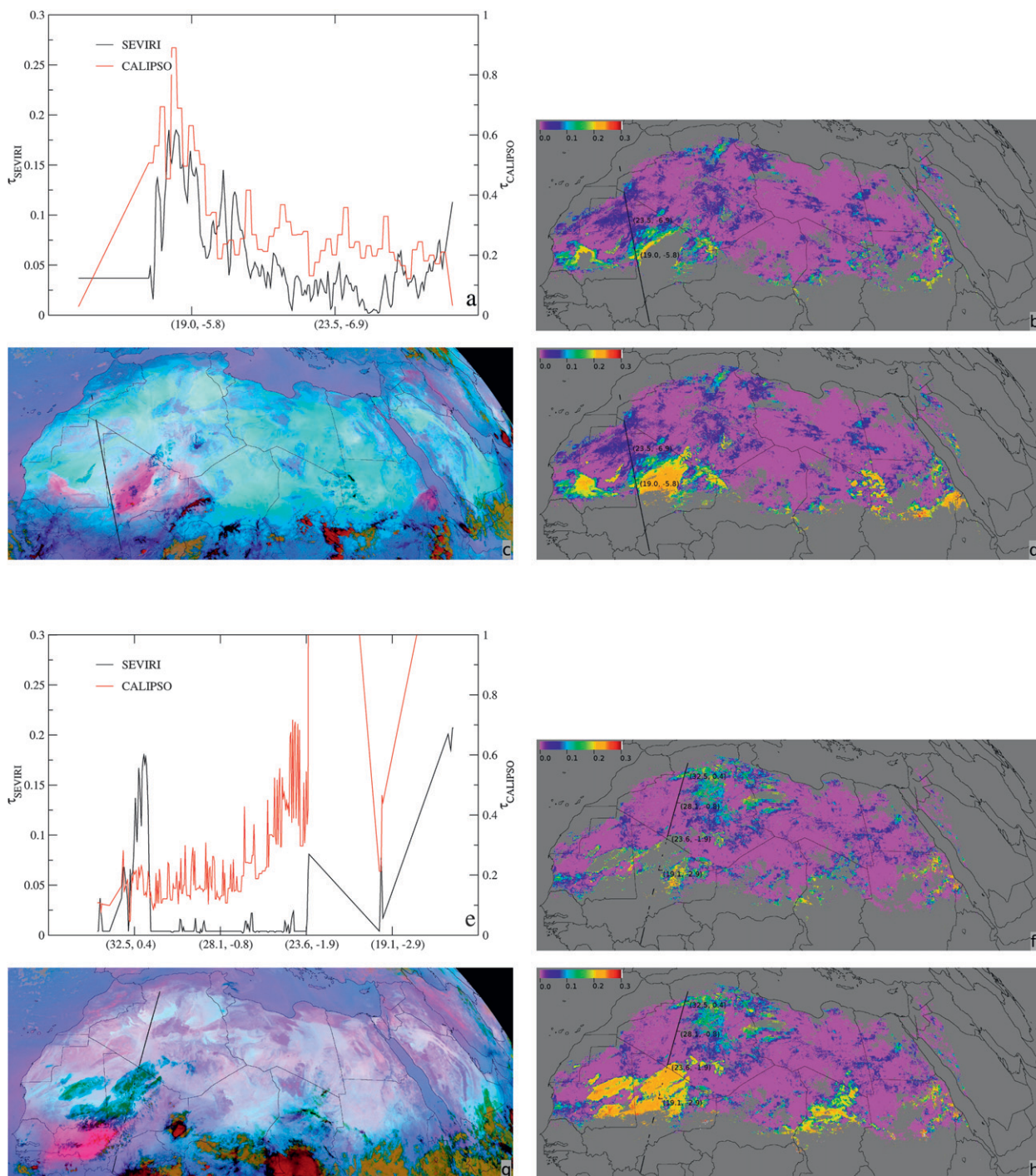


FIG. 7. As in Fig. 5, but for  $\tau_{SEVIRI}$  and  $\tau_{CALIPSO}$  along the CALIPSO track at (a) 1345 UTC 20 Jun 2007 and (e) 0200 UTC 21 Jun 2007.

of both SEVIRI and CALIPSO independently. The origin of the SEVIRI peaks around  $28^{\circ}$ ,  $23.6^{\circ}$ , and  $19.1^{\circ}$ N is due to the surface properties that correspond to the “Grand Erg Oriental,” the “Tassile n’Ajjer” in Algeria, and the “Massif de l’Air” in Niger, respectively.

Figure 7c detects another dust event corresponding to the pink region over Mali. The CALIPSO track passes closely to the west of the plume, resulting in increased  $\tau_{SEVIRI}$  and  $\tau_{CALIPSO}$  around  $19^{\circ}$ N in Fig. 7a. Comparing Figs. 7b,d we observe that the MPEF CM identifies the dust plume as cloud.



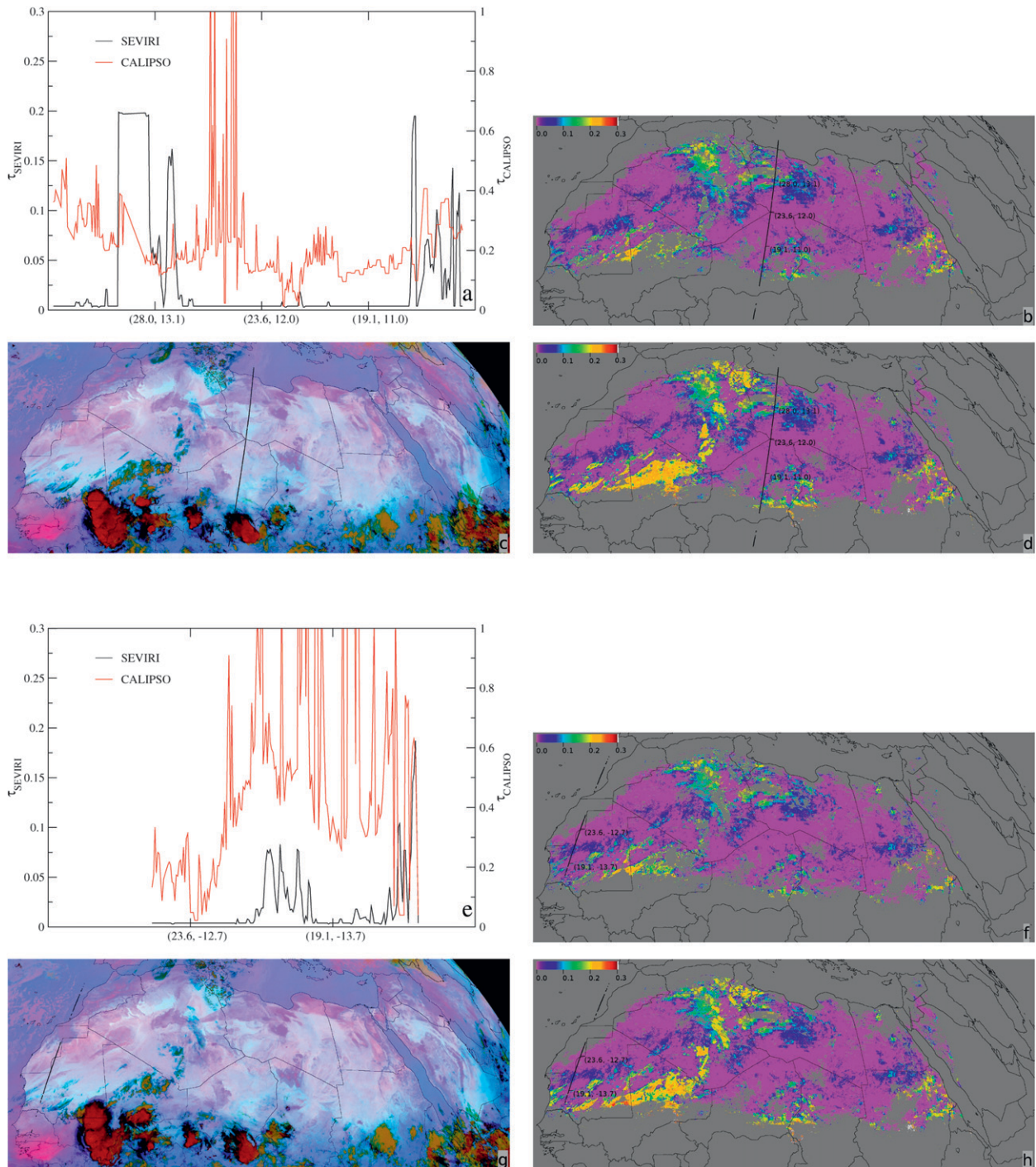


FIG. 8. As in Fig. 5, but for  $\tau_{\text{SEVIRI}}$  and  $\tau_{\text{CALIPSO}}$  along the CALIPSO track at (a) 0115 and (e) 0245 UTC 22 Jun 2007.

In Fig. 7g, almost 12 h after Fig. 7c, the dust plume moved toward Senegal, followed by a large cloudy area that covers Mali. The CALIPSO track crosses this cloudy area south of 23.6°N corresponding to the bad sampling and the high values of both  $\tau_{\text{SEVIRI}}$  and

$\tau_{\text{CALIPSO}}$  in Fig. 7e. The SEVIRI peak at 32.5°N is probably due to the surface properties.

In Fig. 8 the dust plume moved south of Senegal, out of the Sahara region. The CALIPSO track crosses clear sky Sahara surface north of 19.0°N. However, Fig. 8a is

characterized by several peaks of both  $\tau_{\text{SEVIRI}}$  and  $\tau_{\text{CALIPSO}}$ . The SEVIRI peaks are probably due to variations of the surface properties. South of 19.0°N the increasing  $\tau_{\text{SEVIRI}}$  is due to cloud contamination.

In Fig. 8g, only 1 h, 30 min later, the situation is almost the same. The CALIPSO track crosses west of the Sahara that is characterized by the presence of some clouds over Mauritania. Accordingly, both  $\tau_{\text{SEVIRI}}$  and  $\tau_{\text{CALIPSO}}$  increase between 19.0° and 23.6°N due to cloud contamination.

## 9. Conclusions

A new AOD retrieval algorithm over the desert using the SEVIRI window channels is presented. We derive two emissivity ratios using the radiances at 8.7 and at 10.8  $\mu\text{m}$  and the radiances at 8.7 and at 12.0  $\mu\text{m}$ , respectively, and relate the changes in these emissivity ratios to variations of the AOD. Thermal channels observe the aerosols both night and day, allowing their source regions and distribution to be continuously monitored in space and time. The Sahara, the largest desert region on the earth, lies in the middle of Meteosat's field of view, which makes this satellite particularly interesting to use to study dust aerosols. Additionally, desert regions often appear as a gap on the current aerosol retrievals, since their algorithms use the solar channels that are not suited to work over the desert.

This method requires the estimation of the surface emissivity. We derive this parameter by building a clear-sky image that is composed of pixels that have a maximum BT at 10.8  $\mu\text{m}$ , as well as a negative BT difference between the channels at 8.7 and 10.8  $\mu\text{m}$ , selected over a 30-day span. We assume that in this span at least one observation is aerosol and cloud free, and that the surface conditions are constant. Next, this composite image must be corrected for the extinction and emission by the atmosphere to obtain the radiation coming from the surface. This is done by implementing a method from Schmetz (1986) for the window channels, and from Kratz (2005) for the channel at 3.9  $\mu\text{m}$ . We apply the obtained clear-sky apparent surface radiances to a method described by Minnis et al. (2002) to calculate the surface emissivity. We find surface emissivities at 3.9  $\mu\text{m}$  that are low compared to Minnis et al. (2002) and Peres and DaCamara (2005), but that agree well at 8.7, 10.8, and at 12.0  $\mu\text{m}$ . We use the OPAC (Hess et al. 1998) desert model as aerosol input to simulate the thermal IR radiance in the aerosol layer as a function of the wavelength, AOD, surface emissivity, surface temperature, and aerosol layer temperature. From these radiances the emissivity ratios are calculated, which we store in a LUT. These simulations do not account for

gaseous absorption or for clouds, which necessitates that the satellite observations have to be corrected for both. We implemented this algorithm on observations between 19 and 22 June 2007 that were characterized by a minor dust storm over the Sahara. We selected nighttime and daytime observations to take advantage of the possibility of the thermal IR channels to retrieve both at day and at night. We compute the emissivity ratios after correction for the atmospheric absorption and emission of the observed radiances, and match these observed ratios to the simulated ones for the corresponding surface emissivity as a function of surface temperature and aerosol layer temperature to retrieve the  $\tau_{\text{SEVIRI}}$ .

The comparison of the  $\tau_{\text{SEVIRI}}$  with the  $\tau_{\text{CALIPSO}}$  (Figs. 5–8) reveals some weaknesses of the algorithm in the case of background aerosols. The dust RGBs in Figs. 5c,g; 6c,g; 7c,g; and 8c,g reveal similar patterns corresponding to the surface properties. Accordingly, Figs. 5d,h; 6d,h; 7d,h; and 8d,h systematically retrieve increased AOD over places that correspond to these patterns. In particular this is the case for the north of Algeria and Libya. On the other hand, in the presence of dust  $\tau_{\text{SEVIRI}}$  performs quite accurately. Indeed, our detection of a dust event at 1345 UTC 20 June is in agreement with  $\tau_{\text{CALIPSO}}$ . Another dust event at 1300 UTC 19 June is not detected by both SEVIRI and CALIPSO as illustrated in Fig. 6a. We see in Fig. 6c that the area is contaminated by clouds. Therefore the differences of the retrievals between SEVIRI and CALIPSO are due to inaccurate cloud screening.

The inaccuracy due to cloud screening is further illustrated by Figs. 5b,f; 6b,f; 7b,f; and 8b,f, which show the  $\tau_{\text{SEVIRI}}$  masked by the MPEF CM. For all cases where we detected a dust plume, this is partly identified as cloud by the MPEF CM. The current cloud detection algorithms often detect dust aerosols as clouds and vice versa (Brindley and Russel 2006). This correction should be tested itself although there exist dust detection algorithms (Derrien and Le Gléau 2005) that can correct these misidentifications; however, that is the subject of another study. Therefore, the retrieved  $\tau_{\text{SEVIRI}}$  has to be interpreted with care, especially for high AOD above 0.2.

The  $\tau_{\text{SEVIRI}}$  over the desert allows for the completion of missing data continuously in time and space; as such, it is a valuable alternative to the existing AOD products. Improved aerosol models should allow the AOD to be simulated more accurately.

*Acknowledgments.* Special thanks go to the RMIB GERB Team for their support during processing. This paper would not have been possible without the excellent data services of EUMETSAT, RMIB, and ECMWF. The

CALIPSO data were obtained from the NASA Langley Research Center Atmospheric Sciences Data Center. This research was funded by the Belgian Science Policy and hosted by the RMIB.

## REFERENCES

- Ackerman, S. A., 1997: Remote sensing aerosols using satellite infrared observations. *J. Geophys. Res.*, **102**, 17 069–17 079.
- Becker, F., and Z.-L. Li, 1990: Towards a local split window method over land surfaces. *Int. J. Remote Sens.*, **11**, 369–393.
- Brindley, H., and J. Russel, 2006: Improving GERB scene identification using SEVIRI: Infrared dust detection strategy. *Remote Sens. Environ.*, **104**, 426–446.
- Derrien, M., and H. Le Gléau, 2005: MSG/SEVIRI cloud mask and type from SAFNWC. *Int. J. Remote Sens.*, **26**, 4707–4732.
- Diner, D., and Coauthors, 1998: Multi-angle Imaging SpectroRadiometer (MISR) instrument description and experiment overview. *IEEE Trans. Geosci. Remote Sens.*, **36**, 1072–1087.
- Faysash, D. A., and E. A. Smith, 1999: Simultaneous land surface temperature-emissivity retrieval in the infrared split window. *J. Atmos. Oceanic Technol.*, **16**, 1673–1689.
- Hess, M., P. Koepke, and I. Schult, 1998: Optical properties of aerosols and clouds: The software package OPAC. *Bull. Amer. Meteor. Soc.*, **79**, 831–844.
- Hsu, N. C., S.-C. Tsay, M. D. King, and J. R. Herman, 2004: Aerosol properties over bright-reflecting source regions. *IEEE Trans. Geosci. Remote Sens.*, **42** (3), 557–569.
- Husar, R., J. Prospero, and L. Stowe, 1997: Characterization of tropospheric aerosols over the oceans with the NOAA AVHRR optical thickness operational product. *J. Geophys. Res.*, **102**, 16 889–16 909.
- Jiang, G.-M., Z.-L. Li, and F. Nerry, 2006: Land surface emissivity retrieval from combined mid-infrared and thermal infrared data of MSG/SEVIRI. *Remote Sens. Environ.*, **105**, 326–340.
- Kerkmann, J., cited 2004: Dust detection. Tech. Rep. version 1.0, EUMETSAT. [Available online at <http://www.eumetsat.int>.]
- Key, J. R., 2001: Streamer user's guide. Tech. Rep. version 3.0, NOAA/NESDIS, 70 pp. [Available online at <http://stratus.ssec.wisc.edu/streamer/userman.pdf>.]
- King, M. D., Y. J. Kaufman, D. Tanré, and T. Nakajima, 1999: Remote sensing of tropospheric aerosols from space: Past, present, and future. *Bull. Amer. Meteor. Soc.*, **80**, 2229–2259.
- Kratz, D. P., 1995: The correlated k-distribution technique as applied to the AVHRR channels. *J. Quant. Spectrosc. Radiat. Transfer*, **53**, 501–516.
- , cited 2005: Correlated k-distributions for MSG. [Available online at <http://asd-www.larc.nasa.gov/~kratz/msg.html>.]
- Legrand, M., A. Plana-Fattori, and C. N'Doume, 2001: Satellite detection of dust using the IR imagery of Meteosat: 1. Infrared difference dust index. *J. Geophys. Res.*, **106**, 18 251–18 274.
- Li, Z.-H., and F. Becker, 1993: Feasibility of land surface temperature and emissivity determination from AVHRR data. *Remote Sens. Environ.*, **43**, 67–85.
- Loeb, N. G., N. M. Smith, S. Kato, W. F. Miller, S. Gupta, P. Minnis, and B. A. Wielicki, 2003: Angular distribution models for top-of-atmosphere radiative flux estimation from the Clouds and the Earth's Radiant Energy System instrument on the Tropical Rainfall Measuring Mission Satellite. Part I: Methodology. *J. Appl. Meteor.*, **42**, 240–265.
- Lutz, H., 1999: Cloud processing for METEOSAT second generation. Tech. Memo., Vol. 4, EUMETSAT, Darmstadt, Germany, 26 pp.
- Minnis, P., D. F. Young, D. R. Doelling, S. Sun-Mack, Y. Chen, and Q. Z. Trepte, 2002: Surface and clear-sky albedos and emissivities from MODIS and VIRS with application to SEVIRI. *Proc. 2002 EUMETSAT Meteorological Satellite Conf.*, Vol. EUM P 36, Dublin, Ireland, EUMETSAT, 600–607.
- Peres, L. F., and C. C. DaCamara, 2004: Land surface temperature and emissivity estimation based on the two-temperature method: Sensitivity analysis using simulated MSG/SEVIRI data. *Remote Sens. Environ.*, **91**, 377–389.
- , and —, 2005: Emissivity maps to retrieve land-surface temperature from MSG/SEVIRI. *IEEE Trans. Geosci. Remote Sens.*, **43**, 1834–1844.
- Rosenfeld, D., cited 2005: Conversion from counts to radiances and from radiances to brightness temperatures and reflectances. [Available online at [http://oiswww.eumetsat.org/WEBOPS/msg\\_interpretation/PowerPoints/Channels/conversion\\_20050225.ppt](http://oiswww.eumetsat.org/WEBOPS/msg_interpretation/PowerPoints/Channels/conversion_20050225.ppt).]
- Schmetz, J., 1986: An atmospheric-correction scheme for operational application to Meteosat infrared measurements. *ESA J.*, **10**, 145–159.
- , and O. M. Turpeinen, 1988: Estimation of the upper tropospheric relative humidity field from METEOSAT water vapor image data. *J. Appl. Meteor.*, **27**, 889–899.
- , P. Pili, S. Tjemkes, D. Just, J. Kerkmann, S. Rota, and A. Ratier, 2002: An introduction to Meteosat Second Generation. *Bull. Amer. Meteor. Soc.*, **83**, 977–992.
- Slingo, A., and Coauthors, 2006: Observations of the impact of a major Saharan dust storm on the atmospheric radiation balance. *Geophys. Res. Lett.*, **33**, L24817, doi:10.1029/2006GL027869.
- Vaughan, M., S. Young, D. M. Winker, K. Powell, A. Omar, Z. Liu, Y. Hu, and C. A. Hostetler, 2004: Fully automated analysis of space-based lidar data: An overview of the CALIPSO retrieval algorithms and data products. *Laser Radar Techniques for Atmospheric Sensing*, U. Singh, Ed., International Society for Optical Engineering (SPIE Proceedings, Vol. 5575), 16–30.
- Vergé-Dépré, G., M. Legrand, C. Moulin, A. Alias, and P. François, 2006: Improvement of the detection of desert dust over the Sahel using METEOSAT IR imagery. *Ann. Geophys.*, **24**, 1–9.
- Winker, D. M., W. H. Hunt, and C. A. Hostetler, 2004: Status and performance of the CALIOP lidar. *Laser Radar Techniques for Atmospheric Sensing*, U. Singh, Ed., International Society for Optical Engineering (SPIE Proceedings, Vol. 5575), 8–15.
- Wiscombe, W. J., and J. W. Evans, 1977: Exponential-sum fitting of radiative transmission functions. *J. Comput. Phys.*, **24**, 416–444.
- Zhang, P., N. Lu, X. Hu, and C. Dong, 2006: Identification and physical retrieval of dust storms using three MODIS thermal IR channels. *Global Planet. Change*, **52**, 197–206.